

# Microstructure, Phase Transformation, Mechanical Behavior, Bio-corrosion and Antibacterial Properties of Ti-Nb- $x$ Sn ( $x = 0, 0.25, 0.5$ and $1.5$ ) SMAs

Mustafa K. Ibrahim, E. Hamzah, and Safaa N. Saud

(Submitted January 20, 2018; in revised form August 26, 2018; published online November 30, 2018)

Porous Ti-Nb- $x$ Sn shape memory alloys (SMAs) are fabricated by microwave sintering technology. The microstructures exhibit needle-like morphologies,  $\beta_{(N)}$  (normal straight and crossed needles along with needle-like morphology that resembles spaghetti or irregular lines with  $\alpha$ -phases in between) as well as plate-like morphologies [normal straight plate-like morphology,  $\alpha''$  and dendritic plate-like morphology,  $\beta_{(D)}$ ]. Increases in Sn addition significantly induce an increase in the density of the  $\alpha$ -phase. XRD patterns exhibited three phases, namely the  $\beta$ -main phase with smaller intensities of  $\alpha''$  and  $\alpha$ . Further, the addition of 0.25% Sn led to more effective improvement in the intensity of the  $\alpha''$ -phase compared with 0.5% and 1.5% Sn addition. Additions of Sn also enhanced the fracture strength and its corresponding strain along with the shape memory effect (SME), where the best enhancement was achieved at 0.25% Sn. The corrosion rate (Ri) was reduced by rising Sn content, while both corrosion resistance and antibacterial zones were increased. The lower elastic modulus, as well as the robust mechanical properties and bioactivity, made these SMAs rather suitable for biomedical application purposes, where the low elastic modulus had value in terms of avoiding the problem of “stress shielding.”

**Keywords** antibacterial effect, mechanical and corrosion behaviors, microstructure, microwave sintering, porous Ti-Nb- $x$ Sn, shape memory alloys (SMAs)

## 1. Introduction

Pure Ti and Ti alloys have been widely used as implanting materials and for clinical repair based on their excellent mechanical properties, superb corrosion resistance and biocompatibility (Ref 1-6). At present, the elastic modulus of Co-Cr and Ti-6Al-4V is leveraged for orthopedic implant applications, with greater than 100 GPa (Ref 7), while the elastic modulus of the bone is between 4 and 30 GPa depending on measurement direction and bone type (Ref 8, 9). This large difference between bone tissues and implant devices causes stress-shielding problems because of bone resorption (Ref 10), and as such, total hip arthroplasty is necessary based on the loosening of devices. To overcome the critical issue of stress shielding, Ti-Nb-based alloys for biomedical applications have recently attracted much attention, and many alloys with low

elastic modulus as well as robust biocompatibility and high strength have been developed, e.g., Ti-33.6Nb-4Sn (Ref 11), Ti-29Nb-13Ta-4.6Zr (Ref 12), Ti-35Nb-5Ta-7Zr (Ref 13), and Ti-13Nb-13Zr (Ref 14). The existence of pores in titanium alloys reduces the elastic modulus (Ref 15-17) as well as allows for the implant cells to grow into the pores and integrate with the host tissue (Ref 17-19). It was reported by Yang et al. (Ref 16) that porous Ti-(10-35) wt.% Nb alloys were produced by powder metallurgy (PM) technology and featured low elastic modulus (Young's modulus) of 6-15 GPa. Matsumoto et al. (Ref 20) reported that adding Sn to Ti-Nb alloys can enhance the strength of these alloys. It is evident the corrosion rate was reduced after adding Sn, Khalifa et al. (Ref 21) described the presence of Sn with the oxide layer of TiO<sub>2</sub> that improved the effect of this layer in an aggressive environment, enhanced corrosion resistance and diminished the Ri, while Ghoranneviss et al. (Ref 22) noted that pure Sn exhibits antibacterial properties. Ti-Nb-based alloys can be fabricated by PM through several methods, including conventional sintering (Ref 23, 24), metal-injection molding (Ref 25-27), self-propagating high-temperature synthesis (Ref 28), hot-isostatic pressing (Ref 29), spark-plasma sintering (Ref 23, 30, 31) and microwave sintering (MWS). The MWS technique is a relatively new method for preparing Ti-Nb alloys, and it is considered a novel sintering method for metals, composites, ceramics and semi-conductors (Ref 32-34). Overall, MWS has several advantages, such as an enhanced diffusion process, reduced energy and sintering-process time, rapid heating rates and improved mechanical and physical properties (Ref 32, 33). Therefore, the purpose of this study was to evaluate the impact of the amount of Sn on the microstructure characteristics, martensitic transformation, mechanical properties, bio-corrosion and antibacterial effects of Ti-Nb- $x$ Sn SMAs. The results are beneficial for the development of Ti-Nb- $x$ Sn SMAs for biomedical applications.

Mustafa K. Ibrahim and E. Hamzah, Faculty of Mechanical Engineering, Universiti Teknologi Malaysia (UTM), 81310 Johor Bahru, Johor, Malaysia; Safaa N. Saud, Faculty of Information Sciences and Engineering, Management and Science University, Shah Alam, Selangor, Malaysia. Contact e-mails: mustafakhaleel4@gmail.com and esah@fkm.utm.my.

## 2. Experimental Procedure

### 2.1 Sample Preparation

Ti of particle sizes of 45–150  $\mu\text{m}$  and a purity of 99.5% mixed with Nb of a particle size of 74  $\mu\text{m}$  and a purity of 99.85% and a particle size of 45  $\mu\text{m}$  for Sn were utilized. Figure 1 depicts the morphologies of the Ti, Nb and Sn powders. The powders for this research were supplied by Stanford Advanced Materials Company. These powders were prepared for 1 h in a planetary ball mill (PM100) at 300 rpm until becoming well-mixed powder with a weight ratio of ball to powder of 4:1. The  $\text{Ti}_{(77-x)}\text{-Nb}_{23-x}\text{Sn}$  ( $x = 0, 0.25, 0.5, \text{ and } 1.5$ ) were expressed in atomic percentage (at.%); powders were cold-pressed to green samples of  $\Phi 25 \times 10$  mm under a uniaxial pressure of 230  $\text{kg}/\text{cm}^2$  for 5 min followed by MWS (HAMiLab-V3, Synotherm Corp.). These samples underwent MWS at a temperature of 900  $^\circ\text{C}$  for 30 min at a heating rate of 30  $^\circ\text{C}/\text{min}$  and furnace cooling to 250–300  $^\circ\text{C}$ , followed by water cooling (during furnace cooling, the cylindrical stainless steel 304 was under water cooling). The cooling rate at all parameters shows a small range of 8–9  $^\circ\text{C}/\text{min}$ . Next, these samples were coupled with microwaves, where electromagnetic energy was absorbed and transformed into heat to adjust the sintering temperature. An insulation barrel was set up into a continuous 2.45 GHz and 4.5 kV. The sintering was under Ar gas, which fills the sintering chamber with a gas flow purity of 99.999%. The compacts were placed in an alumina crucible surrounded by SiC particles (at the corners of the alumina crucible). SiC was used as an auxiliary heat material. An infrared pyrometer was employed to measure the temperature of the samples during the MWS process.

The sintered samples were cut to dimensions of 7 mm  $\times$  7 mm  $\times$  14 mm using electrical discharge machining (EDM) wire cut for the compression test and 10 mm  $\times$  10 mm  $\times$  20 mm for the shape memory test according to the ASTM E9-09 standards. Corrosion testing was performed with samples of dimensions  $\Phi 13.5 \times 2$  mm while the sample dimension for the antibacterial testing was  $\Phi 5 \times 1.5$  mm.

### 2.2 Microstructural Characterization

Several techniques were used to analyze and characterize the Ti-Nb-xSn SMAs, such as scanning electron microscopy (SEM), x-ray diffraction (XRD), differential scanning calorimetry (DSC), and energy-dispersive x-ray spectroscopy. After cutting, the samples were ground and polished, and this was followed by etching in 10%HF-40%HNO<sub>3</sub>-50% distilled water solution for 15–40 s. SEM (Hitachi Model S-3400N) was employed to evaluate the microstructure. The Archimedes drainage method was utilized to determine the porosity of the samples. The x-ray diffractometer (XRD; D5000 Siemens) was employed to characterize the phase composition of the Ti-Nb-xSn SMAs; the diffraction patterns were identified by Jade software, version 9. The XRD used a  $\text{CuK}\alpha$  x-ray source, and the scanning mode was locked couple with a scan rate of 0.05 $^\circ$ /s and a  $2\theta$  range between 20 and 90  $^\circ\text{C}$ . DSC (DSC; Q200, TA Instrument) was used to determine the phase transformation temperatures of these alloys via the TA Instrument software under heating/cooling rates of 10  $^\circ\text{C}/\text{min}$ . For the DSC test, the temperature ranges were from –80 to 500  $^\circ\text{C}$  in two both heating and cooling cycles and the transformation temperatures

after each cycle nearly the same. The weight of the samples for DSC test was about 10 mg.

### 2.3 Mechanical Tests

An Instron 600 DX-type universal testing machine was used to perform the compression testing at a displacement speed of 0.5 mm/min at 25  $^\circ\text{C}$ . Shape memory test was also performed with an Instron 600 DX-type universal testing machine, which was operated by special program parameters according to the shape memory effect (SME) testing. The loading–unloading cycle compressive test was conducted at a strain of 4%, and moreover, the tests were carried out below the martensite start temperature ( $M_s$ ) to establish shape recovery followed by heating at 200  $^\circ\text{C}$  for 30 min [above austenite finish temperature ( $A_f$ )] with subsequent water quenching. The SME and total strain recovery ( $\varepsilon_T$ ) were calculated by the following forms:  $\text{SME} = (L_f - L_o)/L_f$  and  $\varepsilon_T = (\varepsilon_p - \varepsilon_R)/\varepsilon_p \times 100$ , where  $L_o$  is sample length after compression testing,  $L_f$  is sample length following heating at 200  $^\circ\text{C}$  with water quenching thereafter, ( $\varepsilon_p$ ) is loading–unloading cycle strain, and  $\varepsilon_R$  is residual strain.

### 2.4 Electrochemical Testing/Bio-corrosion

To evaluate the corrosion behavior of Ti-Nb-xSn SMAs, a potentiodynamic polarization (PDP) in a simulated body fluid (SBF) was used. The specimen was connected to an open-air glass cell with a surface area of 0.2  $\text{cm}^2$ , the open-air glass cell contained approximately 300 mL of SBF at a pH of 7.4, and the experiment was accomplished at human body temperature (37  $^\circ\text{C}$ ) with a scan rate of 2 mV/s begun at –250 mV. The VersaSTAT 3 machine (Princeton Applied Research) was used to record the measured data. Each electrochemical test was repeated three times for each sample to ensure the corresponding results. Hereafter, the  $R_i$  and polarization resistance ( $R_p$ ) of these samples was calculated according to (Ref 35, 36) the equations;  $R_i = 22 : 85 i_{\text{corr}}$  and  $R_p = \beta_a \beta_c / (2.3(\beta_a + \beta_c) i_{\text{corr}})$ , where  $i_{\text{corr}}$  is the corrosion current density,  $\beta_c$  is the cathodic Tafel slope and  $\beta_a$  is the anodic Tafel slope. Eventually, the calculations of the output results were based on the polarization curves for the Ti-Nb-xSn SMAs.

### 2.5 Antibacterial Test

The antibacterial activities of metal before and after adding the third alloying element (Sn) were determined by the agar-disk diffusion technique making use of the bacterial species, *Escherichia coli* (gram-negative bacteria) (Ref 37). These bacteria were gotten from the Institute of Medical Research (IMR)/Kuala Lumpur/Malaysia. The glassware was sterilised for 20 min in an autoclave at 120  $^\circ\text{C}$  preceding to the experiment. The stock solution for each organism was produced via mixing 9 mL of Luria–Bertani (LB) broth with 1 mL of each bacterial solution followed by incubation at 37  $^\circ\text{C}$  for 24 h with shaking at 250 rpm. For disk diffusion, solidified nutrient agar media was swabbed with the respective organisms ( $n = 2$ ) ( $1 \times 10^8$  CFU/mL). The disks on each plate were fixed at an equalized distance and incubated at 37  $^\circ\text{C}$  for 24 h. The optimized image was captured with a digital camera. ImageJ software (v 1.47) was used to measure the inhibition zone (mm) around the film.

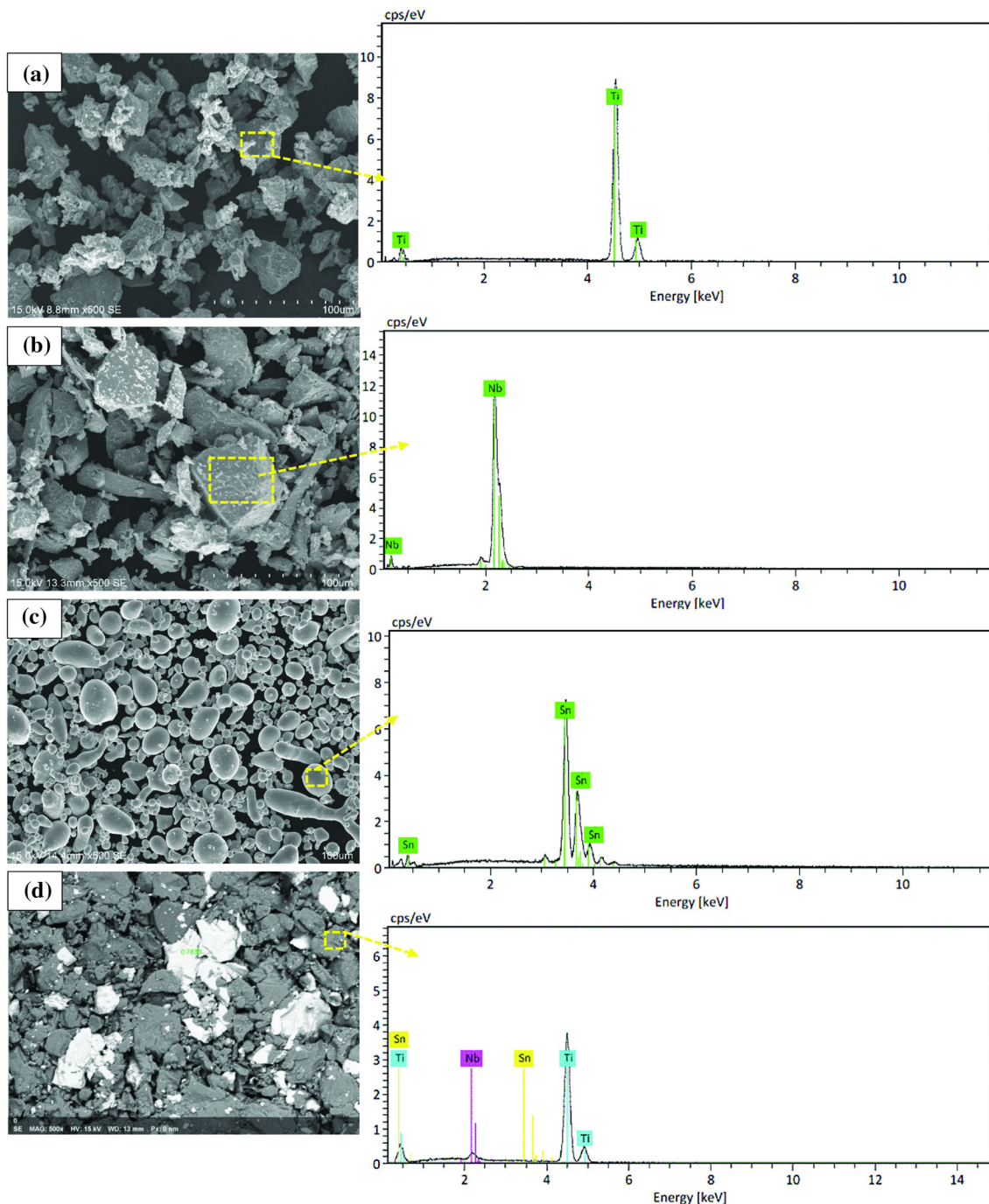


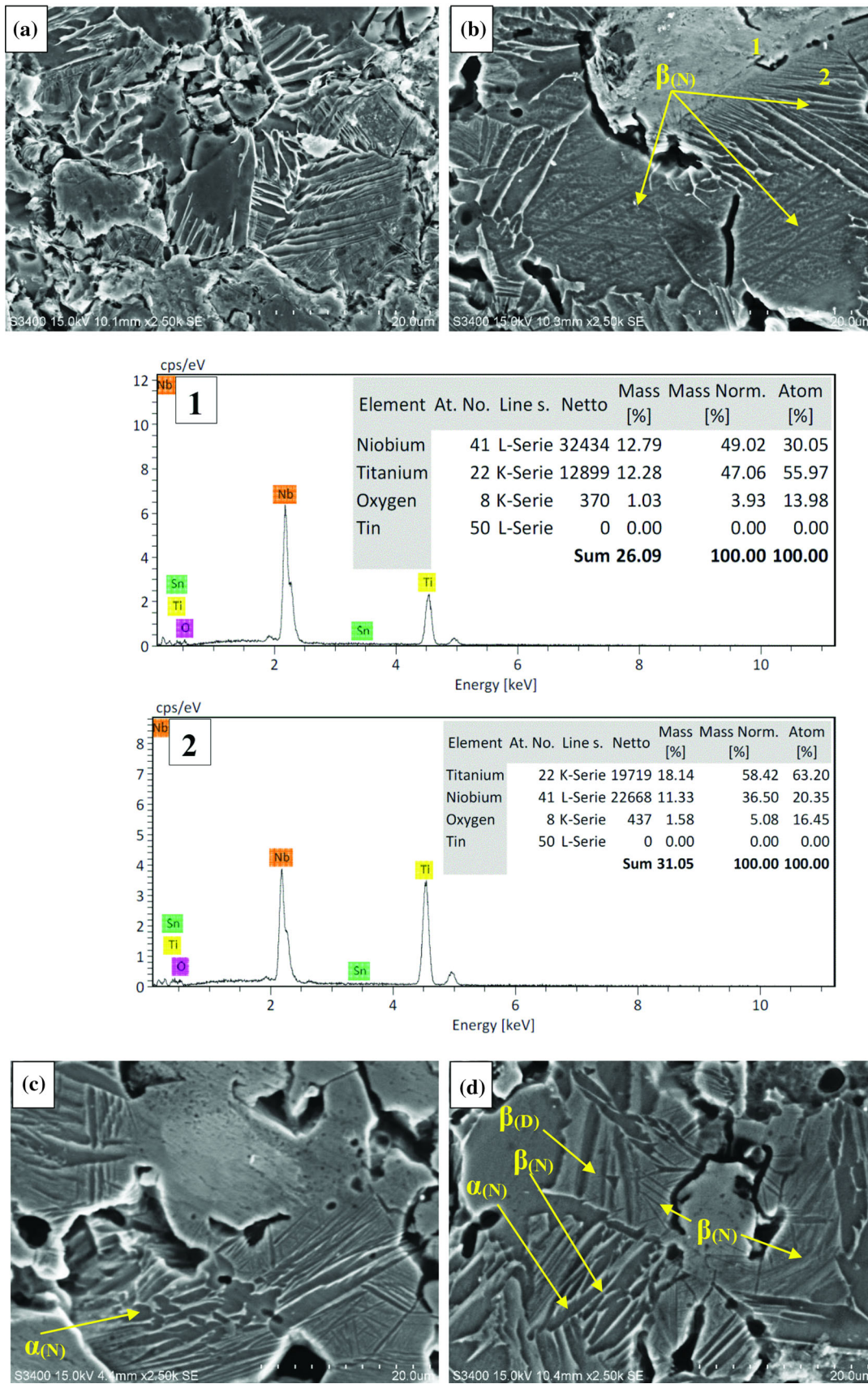
**Fig. 1** SEM micrographs and the corresponding energy-dispersive spectroscopy (EDS) of the powders (a) Ti, (b) Nb, (c) Sn and (d) Ti-Nb-0.25Sn green sample

### 3. Results and Discussion

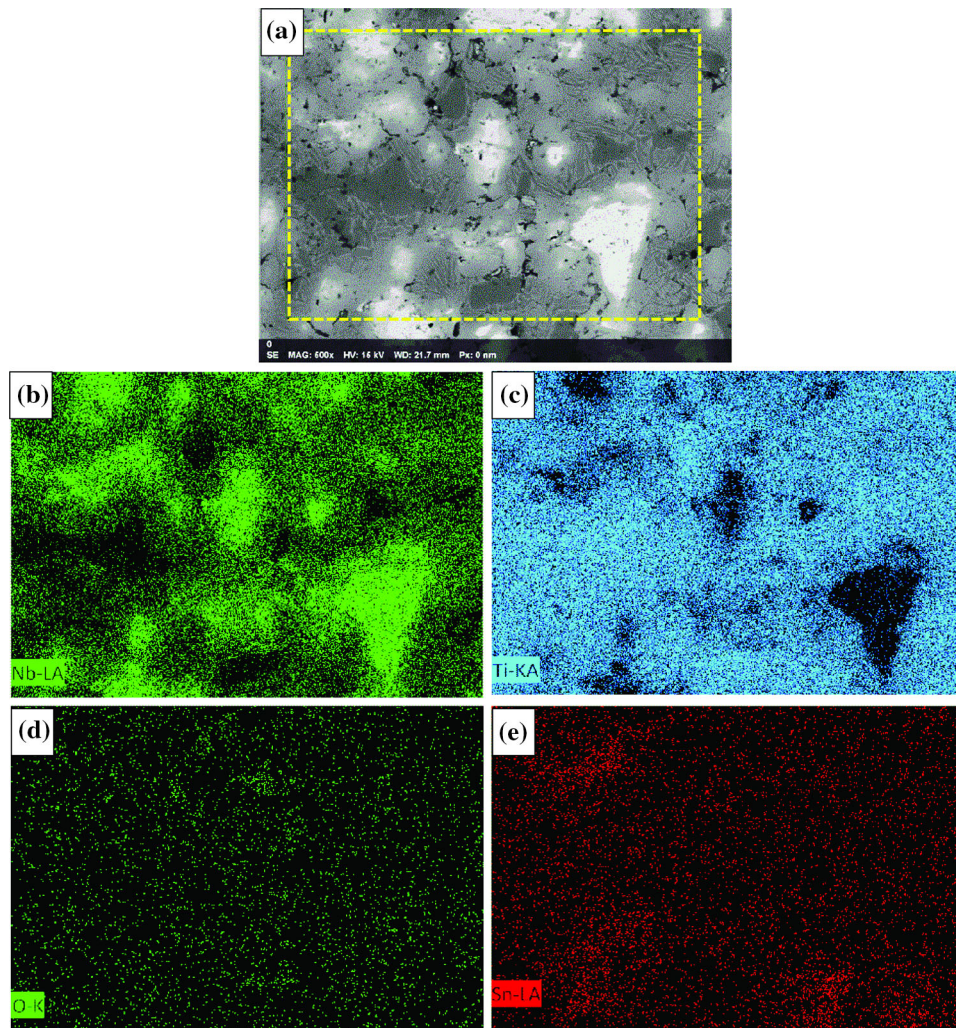
#### 3.1 Microstructure Characteristics

Figure 2 portrays the SEM micrographs of Ti-Nb- $x$ Sn. The microstructures exhibit two forms of morphologies; needle-like morphologies,  $\beta_{(N)}$  (normal straight and crossed needles along with needle-like morphology that resembled spaghetti or irregular lines with  $\alpha$ -phases in between, present with  $\beta$  phase) as well as plate-like morphologies (normal straight plate-like morphology,  $\alpha''$  and dendritic plate-like morphology,  $\beta_{(D)}$ ).

Adding Sn potentially induced an increase in the density of the  $\alpha$ -phase because Sn acts as a  $\alpha$ -Ti stabilizer. Sn hampers the formation of the  $\omega$ -phase and the associated stabilization of the parent  $\beta$ -phase (Ref 38-40). It has been reported that Ti-Nb alloys of 15-35 at.%Nb exhibit superelastic and shape memory properties associated with the  $\beta$  to  $\alpha''$  martensitic transformation (Ref 41), while 20-24 at.%Nb exhibit self-accommodation morphologies of the  $\alpha''$  (Ref 42). It was also described that during the cooling process with a Nb content of  $11 < \text{Nb} < 27$  at.%, the  $\alpha''$  structure forms from the retained  $\beta$ -phase (Ref 43, 44). The titanium structure is HCP ( $\alpha$ ), while niobium



**Fig. 2** SEM micrographs of Ti-Nb-xSn at (a) 0 at.%Sn; (b) 0.25 at.%Sn with EDS analysis at spots 1 and 2; (c) 0.5 at.%Sn; and (d) 1.5 at.%Sn



**Fig. 3** Elemental mapping of the Ti-Nb-0.25%Sn SMA at (a) SEM micrograph, (b) Nb, (c) Ti, (d) O and (e) Sn

structure is BCC ( $\beta$ ). Therefore, Nb-rich region is  $\beta$  phase and the diffusion of Nb to Ti-rich region affects as  $\beta$ -Ti stabilizer, then Ti-rich region is  $(\alpha + \alpha'') + \beta$ . The darkest parts in Ti-rich region contained more  $\alpha$  phase while the less darkness regions or contain needles and plates are  $\beta$  phase except the spaghetti (irregular) shape needles contains  $\alpha$  phase companies with  $\beta$  phase. Furthermore, the SME decreases with increasing precipitates of the equilibrium  $\alpha$ -phase (Ref 45). As well, the density of these alloys was increased gradually with rising amounts of Sn, and these densities were in the range between 77 and 86%. Terayama et al. (Ref 30) reported that elemental additions with lower melting points effectively rose the density of the sintered alloy. Based on EDS, the morphology of the surface exhibited two regions—a bright area related to the Nb-rich region and a dark area referred to as the Ti-rich region (Ref 46, 47). Figure 2(b) portrays the EDS data of Ti-Nb-0.25%Sn, where 1 and 2 indicate the EDS points (spot scanning) on the micrograph in Fig. 2(a). Point 1 refers to Ti with 55.97 at.%Ti and 30.05 at.%Nb associated with an existence of O. Point 2 reflects Ti with 63.20 at.%Ti and 20.35 at.%Nb, with the rest being O. The bright region without the presence of any needle-like or plate-like morphologies refer to the Nb-rich region, while the presence of these morphologies were close to the Ti-rich region and populated the area between the two rich

regions. Sn was not observed at either point. Figure 3 shows the elemental mapping of the Ti-Nb-0.25%Sn SMA with evident diffusion between the elements, and it can be observed there is a Ti-rich region (dark area) and Nb-rich region (bright area). Sn diffused finely in both the Ti and Nb regions.

Figure 4(a) portrays the XRD data of the sintered Ti-23Nb-xSn samples. The influence of Sn on the XRD patterns of Ti-Nb was investigated, and the  $\beta$ ,  $\alpha''$  and  $\alpha$  phases were observed. The main phase was the  $\beta$ -phase that was indicated on planes (110), (200), (211), (112) and (220) at the angles of 38.8°, 55.9°, 70°, 76° and 82.7°, respectively. The  $\alpha''$ -phase appeared at planes (020), (021) and (130) of angles 36.7°, 40.2° and 63°, respectively, while the  $\alpha$ -phase appeared at planes (100), (101), (102), (110) and (201) at angles 35.17°, 40.2°, 52.7°, 63° and 77.12°, respectively. Observation revealed that at 0.25% Sn, there was a slight increase in the intensity of the  $\alpha''$ -phase peak at an angle of 36.7° of plane (020) as well as the peak at an angle of 40.2° containing the largest intensity of the  $\alpha''$ -phase of the plane (021). With a further increase in Sn additions to 0.5% and 1.5%, what resulted was a minor reduction in the intensity of the  $\alpha''$ -phase, which was also reported by Ozaki and Hu (Ref 11, 48), where large amounts of Sn addition in Ti alloys can lead to inadequate occurrence of martensitic transformation. The

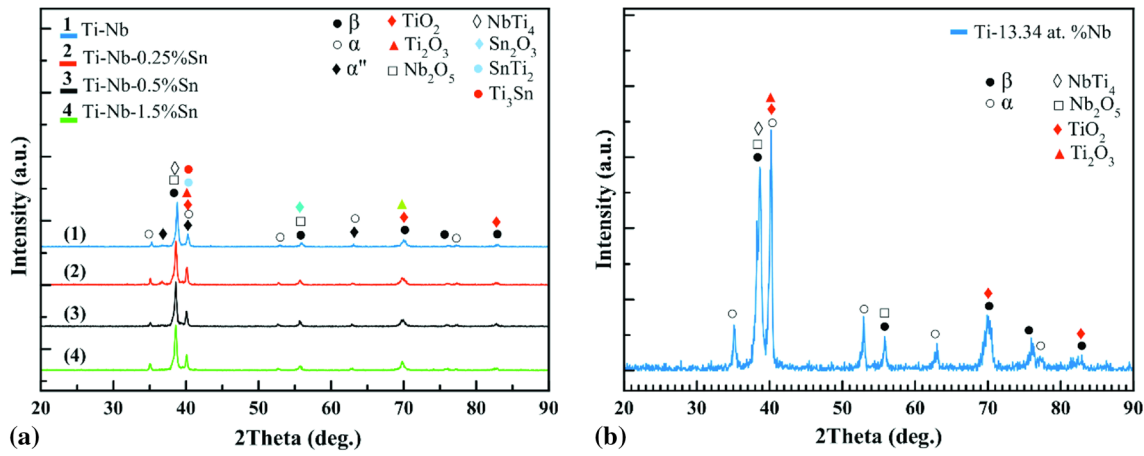


Fig. 4 XRD of samples microwave sintered at 900 °C for 30 min for (a) Ti-23 at.%Nb-xSn SMAs and (b) Ti-13.34 at.%Nb SMA

Table 1 Ti-Nb-Sn transformation temperatures

Alloy	Transformation temperatures, °C			
	$M_s$	$M_f$	$A_s$	$A_f$
Ti-Nb	102.4	100.8	- 37	108
Ti-Nb-0.25 at.%Sn	83.81	82.78	- 49.5	92
Ti-Nb-0.5 at.%Sn	89	88	- 37.86	92
Ti-Nb-1.5 at.%Sn	95.57	94.74	- 25	92

increase in the  $\alpha''$ -phase may have improved the mechanical and shape memory behaviors. Furthermore, there were also many elemental oxides (these oxidize of small intensities due to using argon gas during the sintering process, the oxidation maybe occurs due to the exposing to the atmosphere after furnace cooling to 250-300 °C), such as  $TiO_2$ ,  $Ti_2O_3$ ,  $Nb_2O_5$  and  $Sn_2O_3$ .  $TiO_2$  appeared at planes (022), (112) and (224) of angles 40.2°, 70° and 82.7°, respectively.  $Ti_2O_3$  appeared at plane (113) of an angle 40.2°,  $Nb_2O_5$  appeared at planes (-518) and (017) of angles 38.8° and 55.9°, respectively, while  $Sn_2O_3$  appeared at plane (141) of an angle 55.9°. As well, there were various compounds observed, such as  $NbTi_4$  and  $Ti_3Sn$ .  $NbTi_4$  was located at plane (002) of angle 38.8°,  $Ti_3Sn$  appeared at plane (201) of angle 40.2°. Figure 4(b) portrays the XRD data of the sintered Ti-13.34Nb sample, and the matched phases were the same for the Ti-23Nb alloy (for the  $\beta$  and  $\alpha$  phase, the planes and angles were the same as for the Ti-23Nb alloy, but the  $\alpha''$ -phase was not observed, nor for the oxides and compounds that appeared based on the presence additional Sn). The presence of Nb at 13.34 at.% was less than that in Fig. 4(a), causing an increase in the intensity of the  $\alpha$ -phase, and this may have been because Nb is  $\beta$  stabilizer element (Ref 49). As well, one could not observe the  $\alpha''$ -phase because of the reduction in Nb, which decreased the stability of the  $\beta$ -phase, hence diminishing the  $\alpha''$ -phase that formed from the retained  $\beta$ -phase during cooling, as mentioned previously. It is reported by Lee et al. (Ref 50) that the results indicate that crystal structure and morphology of the Ti-Nb alloys are sensitive to the Nb content.

### 3.2 Transformation Temperatures

Figure 5 features the DSC curves of the Ti-Nb-xSn samples with and without Sn addition, and the extracted data were determined and tabulated in Table 1. It was found that the peak of martensite transformation temperature ( $M_s$  to  $M_f$ ) was shifted to the left to the lowest temperatures with the addition of 0.25% Sn, and this shifting was reduced gradually with rising additional Sn. The range of the austenite transformation temperatures [austenite start temperature ( $A_s$  to  $A_f$ )] became smaller with increasing Sn additions, moderately shifting from  $A_s$  without any changes in the  $A_f$  values. Based on previous research (Ref 11, 48), with a large amount of Sn addition, martensitic transformation has difficulty taking place in Ti alloys potentially because the  $M_s$  and  $M_f$  temperatures (see Table 1) were reduced after adding small amounts of Sn (0.25%) to the Ti-23Nb SMA, while adding greater amounts of Sn (i.e., 0.5% and 1.5%) had smaller effects on  $M_s$  and  $M_f$ . Furthermore, Sn addition may affect the stabilization of Ti-based alloys, thus increasing the stability of the  $\beta$ -phase. This effect of Sn on martensitic transformation was compatible with the fluctuations in the intensities of the  $\alpha''$ -phase in the XRD patterns. In other words, at this temperature, the martensitic transformation will be achieved while applying stress, and hence this martensitic transformation from the  $\beta$ -phase to the martensite  $\alpha''$ -phase will enhance shape memory behavior (Ref 51, 52). There are appearance of peaks not belong to the martensitic transformation during cooling process (see Fig. 5); the reason for the presence of this peak (or peaks) is due to the concentration of different stress regions close to and around the precipitates ( $\alpha$ -precipitates/intermetallic compounds) that are formed during the addition of tin (Ref 53, 54). Based on the Clausius-Clapeyron equation, the presence of stresses in the alloy consistently improves the martensitic transformation temperature. Once martensite forms (Ref 55), the stress field is relaxed near the precipitates and additional martensite transformation inhibited temporarily. Upon further cooling, as the temperature decreases to stress-free martensite start temperature, the martensitic transformation again starts. In this type of transformation, the initial martensite peak increases with greater transformation heat release when compared with the final martensite peak (Ref 56).

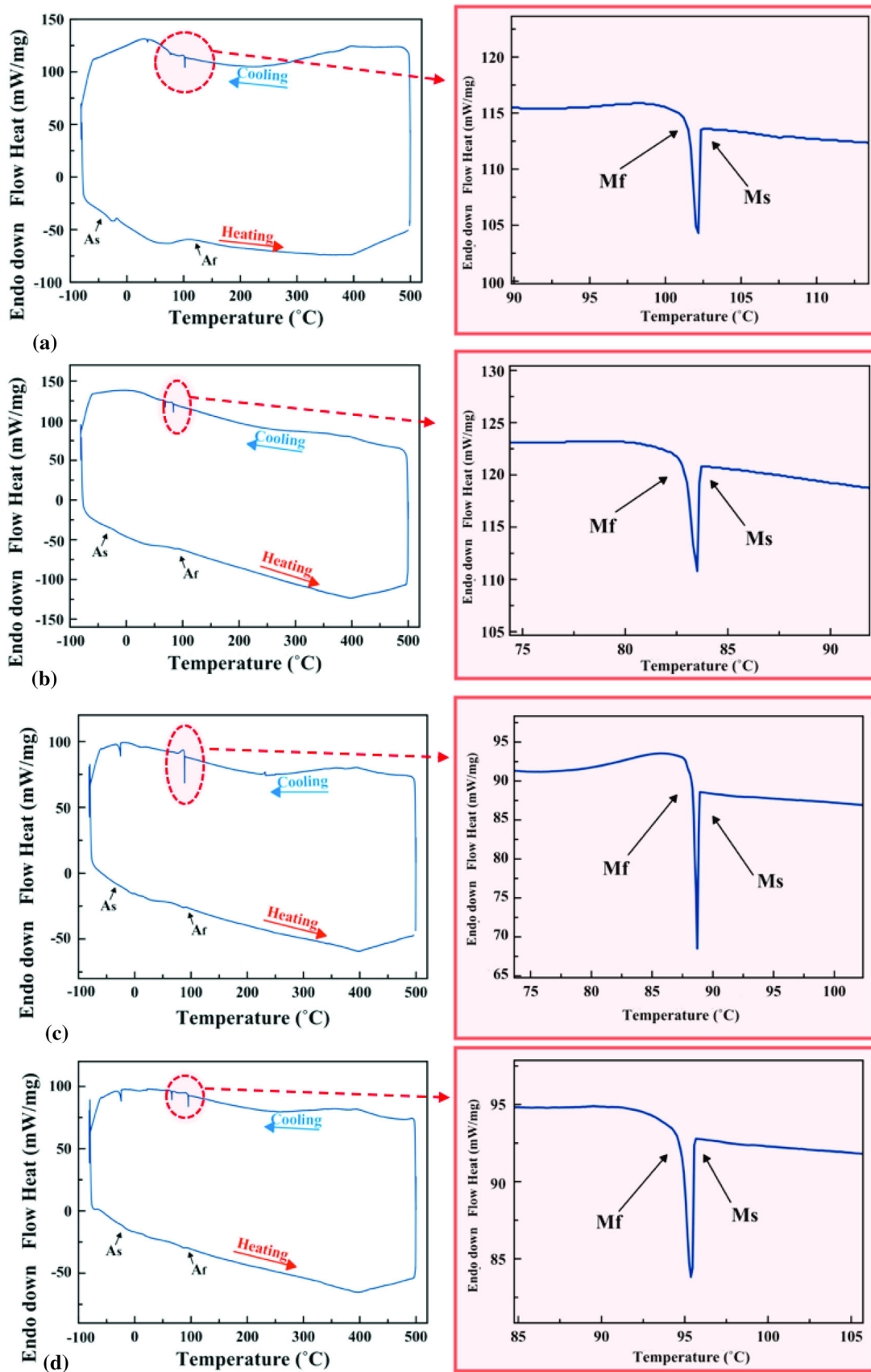


Fig. 5 DSC curves of the Ti-Nb-xSn samples at (a) 0 at.%Sn, (b) 0.25 at.%Sn, (c) 0.5 at.%Sn and (d) 1.5 at.%Sn

### 3.3 Mechanical Properties

**3.3.1 Stress–Strain Curves.** The impact of Sn content on deformation behavior based on compression testing is found in Fig. 6, where all the engineering stress–engineering strain curves of Ti–Nb–Sn exhibit three stages: (a) elastic deformation of the  $\beta$ -austenite; (b) elastic deformation of stress-induced martensite; and (c) plastic deformation of the stress-induced martensite. However, the  $\beta$ -phase can transform into the martensitic  $\alpha''$ -phase by adding stress during loading, while during unloading, the unstable martensitic  $\alpha''$ -phase mostly transforms back into the  $\beta$ -phase (Ref 51). In general, the compression stress of the material decreased with further increases in Sn content as formed via the fracture strain. The sample order of the compression stress and strain was in the sequence of: Ti–Nb–0.25Sn > Ti–Nb–0.5Sn > Ti–Nb–1.5Sn > Ti–Nb. The fraction strength and strain of these SMAs with 0, 0.25, 0.5 and 1.5 at.% Sn were 515 MPa at 26.3%, 643 MPa at 34%, 626 MPa at 30.48% and 589 MPa at 30%, respectively. The highest fracture strength and strain for the Ti–Nb–0.25%Sn alloy were possibly because of the effect of

the amount of Sn on  $\alpha$ -Ti or  $\beta$ -Ti stabilization, where as previously mentioned, Sn acts as  $\alpha$ -Ti stabilizer (Ref 38–40). However, Gutiérrez-Moreno et al. (Ref 57) reported for Ti–Nb alloys that the  $\beta$ -phase was stable at low Sn substitutions, though increasing Sn concentrations induce instability. Therefore, the highest fracture strength and strain were at 0.25% Sn, while greater Sn content caused a slight decrease in fracture strength and its strain. Table 2 presents the effect of Sn addition on maximum stress and its strain, elastic modulus and Vickers hardness. The elastic modulus increased slightly after adding 0.5% Sn content and was reduced slightly at 1.5% Sn, while hardness diminished. The low elastic modulus is utterly important to solving the problem of stress shielding, which occurs based on the significant difference in the elastic modulus of implants and human body tissues (Ref 9, 58, 59). This low elastic modulus was based on the MWS process and its effect on the pores, as well as the low hardness (Ref 15–17).

**3.3.2 Shape Memory Test.** The influence of Sn addition on the shape memory behavior of Ti–Nb–xSn is depicted in Fig. 7. The total strain recovery ( $\epsilon_T$ ) was improved with the addition of Sn compared to the Ti–Nb SMA. The maximum improvement of the  $\epsilon_T$  was observed after adding 0.25 at.% Sn

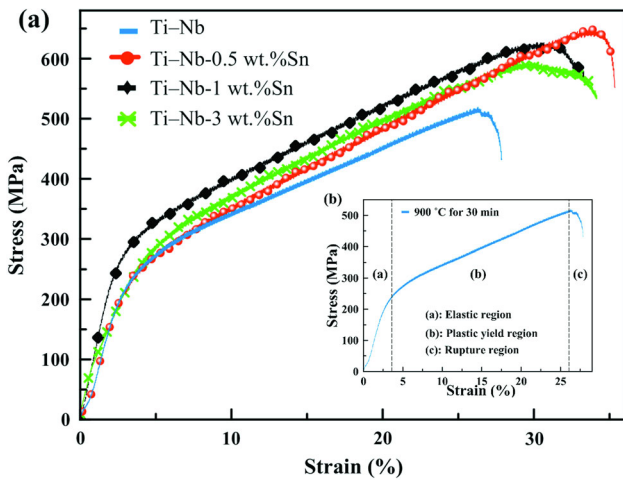


**Fig. 6** Compression test results of (a) Ti–Nb–xSn with different amounts of Sn (b) with the stress–strain curve of the Ti–Nb alloy that exhibits the three stages of this SMA

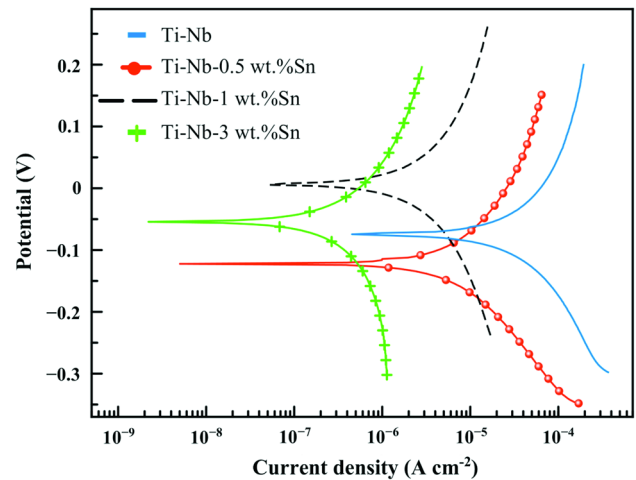


**Fig. 8** PDP curves of Ti–Nb–xSn in SBF solution

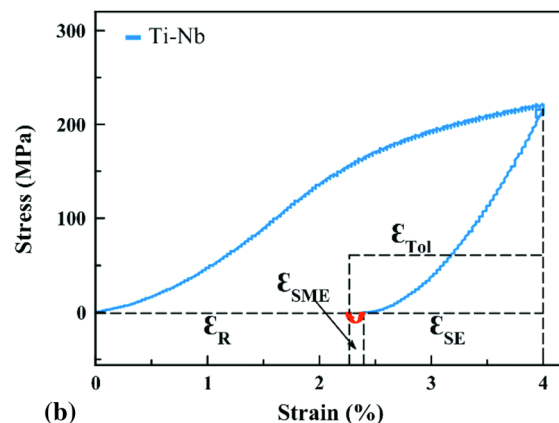
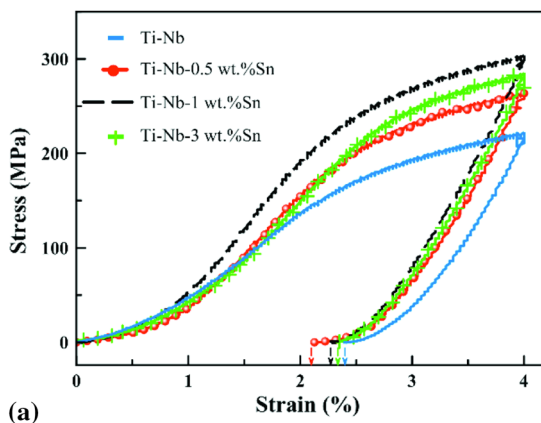


**Fig. 7** Shape-memory test of (a) Ti–23Nb–xSn and (b) Ti–23Nb SMA featuring the  $\epsilon_T$ ,  $\epsilon_R$ ,  $\epsilon_{SME}$  and  $\epsilon_{SE}$



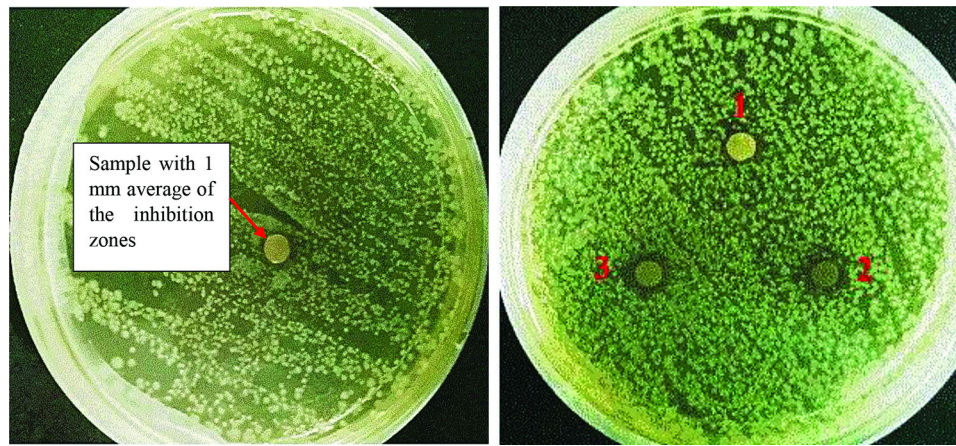


**Fig. 9** Inhibition zones around the Ti-Nb-xSn samples against *E. coli*. On the left hand is 0 at.%Sn while on the right hand is (1) 0.25 at.%Sn, (2) 0.5 at.%Sn and (3) 1.5 at.%Sn

**Table 2** The effect of Sn addition on maximum stress and its strain, elastic modulus and Vickers hardness

Alloys	Maximum strength, $\sigma_{max}$ , MPa	Strain ( $\epsilon_{max}$ ) at maximum strength ( $\sigma_{max}$ ), %	Elastic modulus, $E$ , GPa	Vickers hardness, Hv
Ti-Nb	515 ± 25.75	26.3 ± 1.32	8 ± 0.4	61.7 ± 3
Ti-Nb-0.25 at.%Sn	643 ± 32.15	34 ± 1.7	8 ± 0.4	58.5 ± 3
Ti-Nb-0.5 at.%Sn	626 ± 31.3	30.48 ± 1.5	8.7 ± 0.4	58.7 ± 3
Ti-Nb-1.5 at.%Sn	589 ± 29.5	30 ± 1.5	7.7 ± 0.4	59 ± 3

**Table 3** The residual and total strain of Ti-Nb-xSn SMAs

Alloys	Residual strain, $\epsilon_R$ , %	Total strain recovery ( $\epsilon_T$ ), %
Ti-Nb	2.3785	40.537
Ti-Nb-0.25 at.%Sn	2.122	46.95
Ti-Nb-0.5 at.%Sn	2.282	42.95
Ti-Nb-1.5 at.%Sn	2.314	42.15

**Table 4** Electrochemical parameters of Ti-Nb-xSn samples in SBF solution obtained from polarization test

Alloy	Corrosion potential, $E$ , mV	Current density, $i_{corr}$ , $\mu\text{A}/\text{cm}^2$	Cathodic slope, $\beta_c$ , mV	Anodic slope, $\beta_a$ , mV	Polarization resistance, $R_p$ , k $\Omega$	Corrosion rate, $R_i$ , mm/year
Ti-Nb	- 74.78	55.79	261.875	353.71	1.172	1.2748
Ti-Nb-0.25Sn	- 122.283	9.075	195.406	245.594	5.2136	0.2073
Ti-Nb-0.5Sn	6.413	5.03	378.592	224.973	12.197	0.1149
Ti-Nb-1.5Sn	- 54	0.68	486.005	273.688	111.949	0.0155

to Ti-Nb SMA sintered at 900 °C for 30 min. The  $\epsilon_T$  was reduced with increasing Sn content more than 0.25 at.% Sn. Table 3 features the residual strain ( $\epsilon_R$ ) and  $\epsilon_T$  of the Ti-Nb-xSn SMAs. The  $\epsilon_T$  indicates the percentage of strain recovery by the superelastic recovery and SME (see Fig. 7b). The order of the  $\epsilon_T$  with respect to the samples was: Ti-Nb-0.25Sn > Ti-Nb-0.5Sn > Ti-Nb-1.5Sn > Ti-Nb. The  $\epsilon_T$  of the Ti-Nb-xSn SMAs was determined by utilizing a specially designed compression test at  $T < M_s$  (human body temperature of 37 °C). The  $\epsilon_T$  varied with the changes in the amount of Sn at

the strain value of 4%. The changes in the  $\epsilon_T$  of these SMAs were exhibited after the preheating process at  $T > A_f$ . It was found that the  $\epsilon_T$  rose from 40.537 to 46.95% after adding 0.25 at.%Sn. The increase in Sn addition to more than 0.25 at.% led to a decrease of the  $\epsilon_T$ . Further addition of 0.5 at.% Sn obtained a  $\epsilon_T$  of roughly 42.95%, while 1.5 at.% Sn attained approximately 42.15%. This reduction in  $\epsilon_T$  may be based on Sn precipitates that formed with the addition of Sn. It was proposed that the increase in the amount of Sn addition can result in enhancing  $\alpha$ -phase stability, also may be due to the

influence of Sn addition on the transformation temperatures as mentioned earlier (Ref 11, 48), where small amounts of Sn made the martensite transformation temperatures closer to that of human body temperature of (37 °C). The  $\varepsilon_R$  of these SMAs at  $x = 0, 0.25, 0.5$  and  $1.5$  at.% Sn were 2.3785, 2.122, 2.282 and 2.314, respectively.

### 3.4 Bio-corrosion and Antibacterial Tests

Figure 8 portrays the PDP curves of the Ti-23Nb- $x$ Sn SMAs in SBF solution. Table 4 lists the electrochemical parameters of the Ti-Nb-Sn samples in SBF solution obtained from polarization testing. The current density ( $i_{corr}$ ) values were reduced with increasing Sn addition. The corrosion potential shifted in the noble direction after rising the proportion of Sn from 0.25 to 0.5 at.%, but an elevation to 1.5 at.% Sn diminished the corrosion potential to -54 mV. However, the order of corrosion potential was: Ti-Nb-0.5Sn > Ti-Nb-1.5Sn > Ti-Nb > Ti-Nb-0.25Sn. The order of corrosion rate ( $R_i$ ) based on Sn addition was: Ti-Nb-1.5Sn < Ti-Nb-0.5Sn < Ti-Nb-0.25Sn < Ti-Nb. Ti-Nb-1.5Sn had the highest polarization resistance ( $R_p$ ) compared to the rest of the alloys. However, increasing Sn additions of 0-1.5 at.% rose the  $R_p$  value from 1.172 to 111.949 k $\Omega$ . Therefore, the  $R_p$  of ternary Ti-Nb- $x$ Sn SMAs was observed in the following sequence: Ti-Nb < Ti-Nb-0.25Sn < Ti-Nb-0.5Sn < Ti-Nb-1.5Sn. It was reported by Wu et al. (Ref 60) that adding (0-8) wt.%Sn to Ti<sub>60</sub>Zr<sub>10</sub>Ta<sub>15</sub>Si<sub>15</sub> alloy reduced the corrosion rate and increased the corrosion resistance gradually with increasing Sn content. The antibacterial activity results with the Ti-Nb-Sn samples against *E. coli* are presented in Fig. 9. The average of the inhibition zones for Ti-Nb- $x$ Sn was found to be 1 mm, 1.3 mm, 1.7 mm and 1.9 mm against *E. coli* for 0, 0.25, 0.5 and 1.5 at.%Sn, respectively. The order of the average of the inhibition zones was: Ti-Nb < Ti-Nb-0.25Sn < Ti-Nb-0.5Sn < Ti-Nb-1.5Sn. The average inhibition zone with these SMAs increased with elevated Sn addition; it is reported that tin and its oxides have strong antibacterial effect (Ref 22, 61, 62). The presence of TiO<sub>2</sub> had good antibacterial effects on Ti and its alloys (Ref 63-66), while Nb and Nb oxides moderately enhanced antibacterial properties (Ref 67).

## 4. Conclusions

Based on the data presented, the following conclusions can be drawn:

1. The microstructures exhibited  $\beta_{(N)}$  and  $\beta_{(D)}$  morphologies. The  $\beta_{(N)}$  morphology contained normal straight and crossed needles along with needle-like morphology that resembled spaghetti or irregular lines with  $\alpha$ -phases in between. The plate-like morphology featured normal straight plate-like morphology,  $\alpha''$  and dendritic,  $\beta_{(D)}$ . The XRD patterns of the Ti-23Nb- $x$ Sn SMAs exhibited  $\beta$ ,  $\alpha''$  and  $\alpha$  phases, with  $\beta$ -phase being the main phase with lower intensities of  $\alpha''$  and  $\alpha$  phases. Ti-13.34Nb possessed  $\beta$  and  $\alpha$  phases, with the  $\alpha$ -phase being the primary phase with a lower intensity of the  $\beta$ -phase without any presence of the  $\alpha''$ -phase, potentially because of the effect of Nb as a  $\beta$ -stabilizer.

2. Adding Sn in small amounts (0.25%) improved the martensitic transformation while larger amounts (0.5% and 1.5%) hindered martensitic transformation.
3. Adding Sn improved fracture strength and its strain, with the highest fracture strength and strain being for the Ti-Nb-0.25%Sn SMA. The low elastic modulus and Vickers hardness was based on the MWS process. The low elastic modulus diminished the effect of stress shielding for these SMAs. Further, the SME was enhanced for all Sn additions, but the highest SME was for the Ti-Nb-0.25%Sn SMA.
4.  $R_i$  was reduced gradually with increasing Sn content while corrosion resistance was elevated. The corrosion potential shifted in the noble direction after increasing the proportion of Sn to 0.5 wt.% and 1.5 at.% compared to the Ti-23Nb alloy with less nobility at 0.25%Sn.
5. The average of the inhibition zones of the Ti-Nb- $x$ Sn samples against *E. coli* increased gradually with greater Sn additions. The robust effect of Sn additions on Ti-23Nb SMA made it able to replace the Ti-Ni alloy for biomedical application purposes.

## Acknowledgments

The authors would like to thank the Ministry of Higher Education of Malaysia and Universiti Teknologi Malaysia for providing the financial support under the University Research Grant No. Q.J130000.2524.12H60 and research facilities.

## References

1. X. Wang, Y. Li, J. Xiong, P.D. Hodgson, and C.E. Wen, Porous TiNbZr Alloy Scaffolds for Biomedical Applications, *Acta Biomater.*, 2009, **5**(9), p 3616–3624
2. A. Choubey, R. Balasubramaniam, and B. Basu, Effect of Replacement of V by Nb and Fe on the Electrochemical and Corrosion Behavior of Ti-6Al-4V in Simulated Physiological Environment, *J. Alloy. Compd.*, 2004, **381**(1), p 288–294
3. Y. Tong, B. Guo, Y. Zheng, C.Y. Chung, and L.W. Ma, Effects of Sn and Zr on the Microstructure and Mechanical Properties of Ti-Ta-Based Shape Memory Alloys, *J. Mater. Eng. Perform.*, 2011, **20**(4–5), p 762–766
4. S. Lu, F. Ma, P. Liu, W. Li, X. Liu, X. Chen, K. Zhang, Q. Han, and L.-C. Zhang, Recrystallization Behavior and Super-Elasticity of a Metastable  $\beta$ -Type Ti-21Nb-7Mo-4Sn Alloy During Cold Rolling and Annealing, *J. Mater. Eng. Perform.*, 2018, **27**(8), p 4100–4106
5. T. Ogawa, H. Takada, and K. Maruoka, Corrosion and Mechanical Degradation of Ni-Ti Superelastic Alloy in Neutral Fluoride Solution, *J. Mater. Eng. Perform.*, 2018, **27**, p 1–6
6. Y. Xiao, H. Liu, D. Yi, J. Le, H. Zhou, Y. Jiang, X. Zhao, Z. Chen, J. Wang, and Q. Gao, High-Temperature Deformation Behavior of Ti-6Al-2Sn-4Zr-2Mo Alloy with Lamellar Microstructure Under Plane-Strain Compression, *J. Mater. Eng. Perform.*, 2018, **27**, p 1–14
7. M. Long and H. Rack, Titanium Alloys in Total Joint Replacement—A Materials Science Perspective, *Biomaterials*, 1998, **19**(18), p 1621–1639
8. D.M. Cullinane and T.A. Einhorn, Biomechanics of Bone, *Princ. Bone Biol.*, 2002, **1**, p 16–32
9. M. Geetha, A. Singh, R. Asokamani, and A. Gogia, Ti Based Biomaterials, the Ultimate Choice for Orthopaedic Implants—A Review, *Prog. Mater. Sci.*, 2009, **54**(3), p 397–425
10. H. Kröger, P. Venesmaa, J. Jurvelin, H. Miettinen, O. Suomalainen, and E. Alhava, Bone Density at the Proximal Femur After Total Hip Arthroplasty, *Clin. Orthop. Relat. Res.*, 1998, **352**, p 66–74

11. T. Ozaki, H. Matsumoto, S. Watanabe, and S. Hanada, Beta Ti Alloys with Low Young's Modulus, *Mater. Trans.*, 2004, **45**(8), p 2776–2779
12. D. Kuroda, M. Niinomi, M. Morinaga, Y. Kato, and T. Yashiro, Design and Mechanical Properties of New  $\beta$  Type Titanium Alloys for Implant Materials, *Mater. Sci. Eng., A*, 1998, **243**(1), p 244–249
13. T. Ahmed, A New Low Modulus, Biocompatible Titanium Alloy, in *Titanium'95: Science and Technology* (1996), pp. 1760–1767
14. A.K. Mishra, J.A. Davidson, R.A. Poggie, P. Kovacs, and T.J. FitzGerald, *Mechanical and Tribological Properties and Biocompatibility of Diffusion Hardened Ti-13Nb-13Zr—A New Titanium Alloy for Surgical Implants, Medical Applications of Titanium and its Alloys: The Material and Biological Issues*, ASTM International, West Conshohocken, 1996
15. J. Xu, L. Bao, A. Liu, X. Jin, Y. Tong, J. Luo, Z. Zhong, and Y. Zheng, Microstructure, Mechanical Properties and Superelasticity of Biomedical Porous NiTi Alloy Prepared by Microwave Sintering, *Mater. Sci. Eng., C*, 2015, **46**, p 387–393
16. D. Yang, Z. Guo, H. Shao, X. Liu, and Y. Ji, Mechanical Properties of Porous Ti-Mo and Ti-Nb Alloys for Biomedical Application by Gelcasting, *Proc. Eng.*, 2012, **36**, p 160–167
17. M. Mour, D. Das, T. Winkler, E. Hoenic, G. Mielke, M.M. Morlock, and A.F. Schilling, Advances in Porous Biomaterials for Dental and Orthopaedic Applications, *Materials*, 2010, **3**(5), p 2947–2974
18. A. Bansiddhi, T. Sargeant, S.I. Stupp, and D. Dunand, Porous NiTi for Bone Implants: A Review, *Acta Biomater.*, 2008, **4**(4), p 773–782
19. G. Ryan, A. Pandit, and D.P. Apatidis, Fabrication Methods of Porous Metals for Use in Orthopaedic Applications, *Biomaterials*, 2006, **27**(13), p 2651–2670
20. H. Matsumoto, S. Watanabe, and S. Hanada, Beta TiNbSn Alloys with Low Young's Modulus and High Strength, *Mater. Trans.*, 2005, **46**(5), p 1070–1078
21. O. Khalifa, E. Wahab, and A. Tilp, The Effect of Sn and TiO<sub>2</sub> Nano Particles Added in Electroless Ni-P Plating Solution on the Properties of Composite Coatings, *Aust. J. Basic Appl. Sci.*, 2011, **5**(6), p 136–144
22. M. Ghoranneviss and S. Shahidi, Effect of Various Metallic Salts on Antibacterial Activity and Physical Properties of Cotton Fabrics, *J. Ind. Text.*, 2013, **42**(3), p 193–203
23. M. Wen, C. Wen, P. Hodgson, and Y. Li, Fabrication of Ti-Nb-Ag Alloy Via Powder Metallurgy for Biomedical Applications, *Mater. Des.*, 2014, **56**, p 629–634
24. J. Xiong, Y. Li, X. Wang, P. Hodgson, and C.E. Wen, Mechanical Properties and Bioactive Surface Modification via Alkali-Heat Treatment of a Porous Ti-18Nb-4Sn Alloy for Biomedical Applications, *Acta Biomater.*, 2008, **4**(6), p 1963–1968
25. D. Zhao, K. Chang, T. Ebel, H. Nie, R. Willumeit, and F. Pyczak, Sintering Behavior and Mechanical Properties of a Metal Injection Molded Ti-Nb Binary Alloy as Biomaterial, *J. Alloy. Compd.*, 2015, **640**, p 393–400
26. D. Zhao, K. Chang, T. Ebel, M. Qian, R. Willumeit, M. Yan, and F. Pyczak, Microstructure and Mechanical Behavior of Metal Injection Molded Ti-Nb Binary Alloys as Biomedical Material, *J. Mech. Behav. Biomed. Mater.*, 2013, **28**, p 171–182
27. F. Kafkas and T. Ebel, Metallurgical and Mechanical Properties of Ti-24Nb-4Zr-8Sn Alloy Fabricated by Metal Injection Molding, *J. Alloy. Compd.*, 2014, **617**, p 359–366
28. A. Aleksanyan, S. Dolukhanyan, V.S. Shekhtman, S. Khasanov, O. Ter-Galstyan, and M. Martirosyan, Formation of Alloys in the Ti-Nb System by Hydride Cycle Method and Synthesis of Their Hydrides in Self-Propagating High-Temperature Synthesis, *Int. J. Hydrogen Energy*, 2012, **37**(19), p 14234–14239
29. L.W. Ma, C.Y. Chung, Y. Tong, and Y. Zheng, Properties of Porous TiNbZr Shape Memory Alloy Fabricated by Mechanical Alloying and Hot Isostatic Pressing, *J. Mater. Eng. Perform.*, 2011, **20**(4–5), p 783–786
30. A. Terayama, N. Fuyama, Y. Yamashita, I. Ishizaki, and H. Kyogoku, Fabrication of Ti-Nb Alloys by Powder Metallurgy Process and their Shape Memory Characteristics, *J. Alloy. Compd.*, 2013, **577**, p S408–S412
31. X. Wang, Y. Chen, L. Xu, Z. Liu, and K.-D. Woo, Effects of Sn Content on the Microstructure, Mechanical Properties and Biocompatibility of Ti-Nb-Sn/Hydroxyapatite Biocomposites Synthesized by Powder Metallurgy, *Mater. Des.*, 2013, **49**, p 511–519
32. M. Oghbaei and O. Mirzaee, Microwave Versus Conventional Sintering: A Review of Fundamentals, Advantages and Applications, *J. Alloy. Compd.*, 2010, **494**(1), p 175–189
33. S. Das, A. Mukhopadhyay, S. Datta, and D. Basu, Prospects of Microwave Processing: An Overview, *Bull. Mater. Sci.*, 2009, **32**(1), p 1–13
34. R. Roy, D. Agrawal, J. Cheng, and S. Gedevarishvili, Full Sintering of Powdered-Metal Bodies in a Microwave Field, *Nature*, 1999, **399**(6737), p 668–670
35. H. Bakhsheshi-Rad, M. Idris, M. Abdul-Kadir, A. Ourdjini, M. Medraj, M. Daroonparvar, and E. Hamzah, Mechanical and Bio-corrosion Properties of Quaternary Mg-Ca-Mn-Zn Alloys Compared with Binary Mg-Ca Alloys, *Mater. Des.*, 2014, **53**, p 283–292
36. G. Argade, K. Kandasamy, S. Panigrahi, and R. Mishra, Corrosion Behavior of a Friction Stir Processed Rare-Earth Added Magnesium Alloy, *Corros. Sci.*, 2012, **58**, p 321–326
37. N. Iqbal, M.R.A. Kadir, N.H.B. Mahmood, S. Iqbal, D. Almasi, F. Naghizadeh, H. Balaji, and T. Kamarul, Characterization and Biological Evaluation of Silver Containing Fluoroapatite Nanoparticles Prepared Through Microwave Synthesis, *Ceram. Int.*, 2015, **41**(5), p 6470–6477
38. P.J.S. Buenconsejo, H.Y. Kim, and S. Miyazaki, Effect of Ternary Alloying Elements on the Shape Memory Behavior of Ti-Ta Alloys, *Acta Mater.*, 2009, **57**(8), p 2509–2515
39. P.J.S. Buenconsejo, H.Y. Kim, and S. Miyazaki, Novel  $\beta$ -TiTaAl Alloys with Excellent Cold Workability and a Stable High-Temperature Shape Memory Effect, *Scripta Mater.*, 2011, **64**(12), p 1114–1117
40. H.Y. Kim, T. Fukushima, P.J.S. Buenconsejo, T.-H. Nam, and S. Miyazaki, Martensitic Transformation and Shape Memory Properties of Ti-Ta-Sn High Temperature Shape Memory Alloys, *Mater. Sci. Eng., A*, 2011, **528**(24), p 7238–7246
41. H. Kim, Y. Ikehara, J. Kim, H. Hosoda, and S. Miyazaki, Martensitic Transformation, Shape Memory Effect and Superelasticity of Ti-Nb Binary Alloys, *Acta Mater.*, 2006, **54**(9), p 2419–2429
42. Y. Chai, H. Kim, H. Hosoda, and S. Miyazaki, Self-Accommodation in Ti-Nb Shape Memory Alloys, *Acta Mater.*, 2009, **57**(14), p 4054–4064
43. J.L. Murray, The Nb-Ti (Niobium-Titanium) System, *Bull. Alloy Phase Diagr.*, 1981, **2**(1), p 55–61
44. H.Y. Kim and S. Miyazaki, Martensitic Transformation and Superelastic Properties of Ti-Nb Base Alloys, *Mater. Trans.*, 2015, **56**(5), p 625–634
45. Y. Guo, beta-bcc and Amorphous Ti-Based Biocompatible Alloys for Human Body Implants, Université Grenoble Alpes, 2014
46. B. Sharma, S.K. Vajpai, and K. Ameyama, Microstructure and Properties of Beta Ti-Nb Alloy Prepared by Powder Metallurgy Route Using Titanium Hydride Powder, *J. Alloy. Compd.*, 2016, **656**, p 978–986
47. A. Nouri, J. Lin, Y. Li, Y. Yamada, P. Hodgson, C. Wen, Microstructure Evolution of Ti-Sn-Nb Alloy Prepared by Mechanical Alloying, in *Materials Forum (CD-ROM)*, 2007, Institute of Materials Engineering Australasia, pp. 64–70
48. Q.-M. Hu, S.-J. Li, Y.-L. Hao, R. Yang, B. Johansson, and L. Vitos, Phase Stability and Elastic Modulus of Ti Alloys Containing Nb, Zr, and/or Sn from First-Principles Calculations, *Appl. Phys. Lett.*, 2008, **93**(12), p 121902
49. Y. Guo, K. Georganakis, Y. Yokoyama, and A. Yavari, On the Mechanical Properties of TiNb Based Alloys, *J. Alloy. Compd.*, 2013, **571**, p 25–30
50. C. Lee, C.-P. Ju, and J. Chern Lin, Structure-Property Relationship of Cast Ti-Nb Alloys, *J. Oral Rehabil.*, 2002, **29**(4), p 314–322
51. R.P. Kolli, W.J. Joost, and S. Ankem, Phase Stability and Stress-Induced Transformations in Beta Titanium Alloys, *JOM*, 2015, **67**(6), p 1273–1280
52. S. Ehtemam-Haghighi, Y. Liu, G. Cao, and L.-C. Zhang, Influence of Nb on the  $\beta \rightarrow \alpha$  Martensitic Phase Transformation and Properties of the Newly Designed Ti-Fe-Nb Alloys, *Mater. Sci. Eng., C*, 2016, **60**, p 503–510
53. N. Vellios and P. Tsakirooulos, The Role of Sn and Ti Additions in the Microstructure of Nb-18Si Base Alloys, *Intermetallics*, 2007, **15**(12), p 1518–1528
54. I. Gorna, M. Bulanova, K. Valuiska, M. Bega, O.Y. Koval, A. Kotko, Y.I. Evich, and S. Firstov, Alloys of the Ti-Si-Sn System (Titanium Corner): Phase Equilibria, Structure, and Mechanical Properties, *Powder Metall. Met. Ceram.*, 2011, **50**(7–8), p 452–461
55. M. Kato and H.R. Pak, Thermodynamics of Stress-Induced First-Order Phase Transformations in Solids, *Phys. Status Solidi B*, 1984, **123**(2), p 415–424

56. T.T. Sasaki, B.C. Hornbuckle, R.D. Noebe, G.S. Bigelow, M.L. Weaver, and G.B. Thompson, Effect of Aging on Microstructure and Shape Memory Properties of a Ni-48Ti-25Pd (At. Pct) Alloy, *Metall. Mater. Trans. A*, 2013, **44**(3), p 1388–1400
57. J. Gutiérrez-Moreno, Y. Guo, K. Georgarakis, A. Yavari, G. Evangelakis, and C.E. Lekka, The Role of Sn Doping in the  $\beta$ -Type Ti-25 at.% Nb Alloys: Experiment and Ab Initio Calculations, *J. Alloy. Compd.*, 2014, **615**, p S676–S679
58. J. Nagels, M. Stokdijk, and P.M. Rozing, Stress Shielding and Bone Resorption in Shoulder Arthroplasty, *J. Shoulder Elbow Surg.*, 2003, **12**(1), p 35–39
59. M. Niinomi, Metallic Biomaterials, *J. Artif. Organs*, 2008, **11**(3), p 105–110
60. X. Wu, Q. Peng, J. Zhao, and J. Lin, Effect of Sn Content on the Corrosion Behavior of Ti-Based Biomedical Amorphous Alloys, *Int. J. Electrochem. Sci.*, 2015, **10**, p 2045–2054
61. S.M. Amininezhad, A. Rezvani, M. Amouheidari, S.M. Amininejad, and S. Rakhshani, The Antibacterial Activity of SnO<sub>2</sub> Nanoparticles Against *Escherichia coli* and *Staphylococcus aureus*, *Zahedan J. Res. Med. Sci.*, 2015, **17**(9), p e1053
62. P. Kamaraj, R. Vennila, M. Arthanareeswari, and S. Devikala, Biological Activities of Tin Oxide Nanoparticles Synthesized Using Plant Extract, *Pharm. Pharm. Sci.*, 2014, **3**, p 338–382
63. L.H. Yun Lu, Y. Hirakawa, and H. Sato, Antibacterial Activity of TiO<sub>2</sub>/Ti Composite Photocatalyst Films Treated by Ultrasonic Cleaning, *Adv. Mater. Phys. Chem.*, 2012, **2**, p 9–12
64. Y.S. Kim, E.S. Park, S. Chin, G.-N. Bae, and J. Jung, Antibacterial Performance of TiO<sub>2</sub> Ultrafine Nanopowder Synthesized by a Chemical Vapor Condensation Method: Effect of Synthesis Temperature and Precursor Vapor Concentration, *Powder Technol.*, 2012, **215**, p 195–199
65. Y.L. Zhou, M. Niinomi, T. Akahori, H. Fukui, and H. Toda, Corrosion Resistance and Biocompatibility of Ti-Ta Alloys for Biomedical Applications, *Mater. Sci. Eng., A*, 2005, **398**(1), p 28–36
66. R. Ahmad and M. Sardar, TiO<sub>2</sub> Nanoparticles as an Antibacterial Agents Against *E. coli*, *Int. J. Innov. Res. Sci. Eng. Technol.*, 2013, **2**(8), p 3569–3574
67. G. Ramirez, S. Rodil, H. Arzate, S. Muhl, and J. Olaya, Niobium Based Coatings for Dental Implants, *Appl. Surf. Sci.*, 2011, **257**(7), p 2555–2559